

Electrochemical behavior of spray deposited mixed nickel manganese oxide thin films for supercapacitor applications

Uday J. Chavan¹ · Abhijit A. Yadav¹

Received: 11 November 2016 / Accepted: 25 November 2016 / Published online: 2 December 2016
© Springer Science+Business Media New York 2016

Abstract The relatively low energy density is a crucial issue obstructing the growth of supercapacitors as energy storage devices. Various tactics have been developed to enhance the energy density. Nickel manganese oxide thin films have been synthesized by spray pyrolysis on pre-heated amorphous and FTO coated glass substrates. These films are characterized for structural, morphological and optical properties using X-ray diffraction, scanning electron microscopy and UV–Vis spectrophotometer. XRD study illustrates formation of spinel cubic NiMn_2O_4 as prominent phase with crystalline size 11 nm. SEM shows fractured surface morphology; wherein small pores on the surface are covered by the particles. Optical band gap of 1.98 eV is observed. The electrochemical performance of NiMn_2O_4 electrode is studied by cyclic voltammetry, galvanostatic charge/discharge and electrochemical impedance spectroscopy measurements. The maximum specific capacitance is found to be 460 Fg^{-1} at scan rate of 5 mVs^{-1} . The excellent rate capability and long term stability suggests NiMn_2O_4 thin film to be good candidate for electrochemical supercapacitors.

1 Introduction

In twenty-first century the appeal for use of unpolluted and renewable energy storage devices has triggered attention due to lack of fossil fuels and the serious environmental

problems [1]. It gives immense challenge to investigate high performance, low-cost and environmental friendly energy storage devices needed for modern civilization [1]. This can be achieved by clean energy sources and carriers, including hydrogen storage, lithium batteries and supercapacitors [2]. Amongst these, supercapacitors have attracted more attention due to their unique characteristics such as enormous power density, good reversibility, low maintenance cost, high cycling stability and environmental friendliness [3, 4]. Furthermore, supercapacitors fill the gap between conventional capacitors and secondary batteries. On the basis of energy storage mechanism supercapacitors are categorized into two groups: electric double layer capacitors (EDLCs) and pseudocapacitors. In EDLCs charges are stored by forming electric double layer of ions at the electrode–electrolyte interfaces while in pseudocapacitors charges are stored by redox reactions occurring on the surface of the electrode [5].

Carbon based materials like activated carbons, carbon nanotubes and graphene belong to EDLC's and transition metal oxides/hydroxides as well as conductive polymers are pseudocapacitive [6]. The transition metal oxides provide superior electrochemical performance with high specific capacitances and good electrochemical stability [7]. RuO_2 based supercapacitors show good electrochemical performance, but suffer from high material cost and toxicity [8]. Therefore its comprehensive production is not beneficial. Other low-cost transition metal oxides such as SnO_2 , MnO_x , NiO , CuO_x , Co_3O_4 , Fe_2O_3 , TiO_2 , MoO_2 , and VO_x are considered as ideal electrode materials in electrochemical supercapacitors [9–11]. Mn_3O_4 and NiO materials have been studied extensively due to their superior electrochemical performance in pseudocapacitor as compared with carbon based materials. Mn_3O_4 and NiO electrodes show low specific capacitance due to its poor electrical conductivity.

✉ Abhijit A. Yadav
aay_physics@yahoo.co.in

¹ Thin Film Physics Laboratory, Department of Physics, Electronics and Photonics, Rajarshi Shahu Mahavidyalaya, Latur (Autonomous), Maharashtra 413512, India

The mixed transition metal oxides are the possible way to overcome this limitation [12]. Recently, the Mn and Ni based mixed transition metal oxides like MnFe_2O_4 , MnMoO_4 , NiCo_2O_4 , and NiMoO_4 were studied for electrochemical supercapacitor electrodes [13]. Ternary oxide, NiMn_2O_4 is one of the best candidates for supercapacitors. The amalgamation of nickel in manganese oxide apparently acts on the resistivity and surface area of the material [12].

Previously, Lee and coworkers [14] have reported electrodeposited manganese–nickel oxide films on a graphite sheet confirming separate manganese oxide ($\gamma\text{-MnO}_2$) and nickel oxide (NiO) phases. Specific capacitance exhibited by these films is observed to be 424 Fg^{-1} in Na_2SO_4 electrolyte. Ahuja et al. [15] have synthesized nickel manganese mixed oxide by in situ inclusion for supercapacitor applications. At Ni/Mn ~ 0.25 the material crystallizes into spinel NiMn_2O_4 as a prominent phase and exhibits specific capacitance of 380 Fg^{-1} . Nanostructured spinel NiMn_2O_4 electrodes were fabricated by Wei et al. [16]. These electrodes exhibited specific capacitances of 662.5 Fg^{-1} in 6 M KOH and 370.5 Fg^{-1} in 1 M Na_2SO_4 at the current density of 1 Ag^{-1} .

There are various methods adopted for the synthesis of nanostructured NiMn_2O_4 thin films. Zhang et al. [17] have used sol gel process for preparation of spinel NiMn_2O_4 thin films at 300°C . Goto et al. [18] have prepared NiMn_2O_4 by conventional heating solid state reaction and irradiated with a microwave magnetic field under air. The other methods used for preparation NiMn_2O_4 are solution growth [19], hydrothermal and spray pyrolysis [20–22]. Spray pyrolysis technique was employed for deposition of spinel NiMn_2O_4 on glass substrates at 350°C by Larbi et al. [22]. However, the demand for simple and low cost preparation process and superior performance of NiMn_2O_4 material still remains a challenge.

In this work, we have synthesized ternary nickel manganese oxide (NiMn_2O_4) thin films by computerized spray pyrolysis. Structural, morphological and optical properties of NiMn_2O_4 thin films have been investigated. The electrochemical performance is studied using cyclic voltammetry, galvanostatic charge/discharge and electrochemical impedance spectroscopy in 2 M aqueous KOH electrolyte. Moreover, NiMn_2O_4 based supercapacitor showed maximum specific capacitance of 460 Fg^{-1} at 5 mVs^{-1} , a maximum energy density of 36.65 Whkg^{-1} at power density of 1.54 kWkg^{-1} and 92.97% capacitance retention after 1000 cycles at current density of 2 Ag^{-1} .

2 Experimental

The equimolar (0.5 M) AR grade manganese acetate [$\text{Mn}(\text{CH}_3\text{COO})_2 \cdot 4\text{H}_2\text{O}$] and Nickel chloride ($\text{NiCl}_2 \cdot 6\text{H}_2\text{O}$)

were used as precursors. The precursor volume ratio of Ni:Mn used was 1:2. Mixed solutions are then sprayed through a fine nozzle with 0.5 mm diameter onto a preheated amorphous glass and FTO substrates. Substrate temperature was fixed at its optimized value of 400°C . The nozzle to substrate distance was fixed at 30 cm. Air was used as the carrier gas. Spray rate was maintained at $3\text{--}4 \text{ ml min}^{-1}$ throughout the experiment.

Structural, morphological and optical properties of the NiMn_2O_4 thin films are studied using X-ray diffraction (XRD), scanning electron microscopy (SEM) and UV–Visible (UV–Vis) spectrophotometer. XRD measurements are carried out via Bruker-AXS D8 ADVANCE X-ray diffractometer at 40 kV voltage and 40 mA current with Cu-K_α radiation. Surface morphology of samples is examined with the help of JEOL-JSM 5600 scanning electron microscope. The spectral absorbance of the NiMn_2O_4 thin film is recorded, in the wavelength range of 300–1100 nm, using SHIMADZU UV-1700 UV–Vis spectrophotometer. Electrochemical measurements are performed in three-electrode system electrochemical analyzer 608D provided by CH Instruments. A NiMn_2O_4 thin film acts as working electrode, Pt foil as a counter electrode, and an Ag/AgCl as a reference electrode. Cyclic voltammetry (CV), galvanostatic charge/discharge (GCD) and electrochemical impedance spectroscopy (EIS) studies are performed in the 2 M aqueous KOH electrolyte.

3 Results and discussion

3.1 X-ray diffraction

Structural properties of the NiMn_2O_4 thin film are investigated using XRD. Figure 1 shows XRD pattern of NiMn_2O_4 thin film deposited at 400°C . The broader and less intense peaks indicate less crystallinity of the NiMn_2O_4 thin film. The peaks are observed at 29.0° , 36.1° , 46.6° , 74.1° corresponding to (220), (222), (311), (533) planes respectively stand for cubic NiMn_2O_4 phase and peaks at 32.2 , 44.3 , 51.2 , 60.4 and 68.0 correspond to (103), (220), (105), (224) and (411) planes of Mn_3O_4 Hausmannite phase. Similar mixed phase structures were also observed by Ma et al. [23] and Gao et al. [24] when the precursor is calcined at different temperatures. The poor crystalline nature and mixed phase indicate incomplete transformation of precursor to NiMn_2O_4 phase as the deposition takes place at lower substrate temperature. From Table 1 it is observed that calculated ‘d’ values are well matched with standard ‘d’ values for mixed nickel

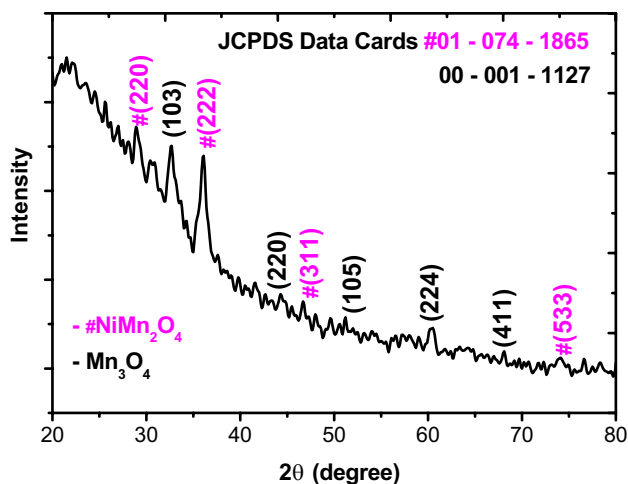


Fig. 1 XRD pattern of NiMn₂O₄ thin film spray deposited at 400 °C

Table 1 Structural properties of mixed nickel manganese oxide thin film

2θ	dstd (Å)	dcal (Å)	hkl	D (nm)
28.95	3.0506	2.9708	220	11
32.53	2.7149	2.7500	103	
36.09	2.4471	2.4256	222	
44.28	1.9945	2.0300	220	
46.59	1.8956	1.9277	311	
51.20	1.7249	1.7900	105	
60.43	1.4614	1.5400	224	
68.08	1.2972	1.3800	411	
74.12	1.1915	1.2814	533	

θ Bragg's angle, d interplanar spacing, hkl miller indices, D crystalline size

manganese oxide. The lattice parameters are calculated using the relation;

$$d = \frac{a}{\sqrt{(h^2 + k^2 + l^2)}} \quad (1)$$

where d is the interplanar spacing, a = lattice parameter and h, k, l are the miller indices. The estimated lattice constant $a=b=c=8.47$ Å is close to standard value 8.40 Å. Crystalline size (D) for plane (222) is calculated with Scherrer's equation;

$$D = \frac{k\lambda}{\beta \cos\theta} \quad (2)$$

where k is the constant, λ is the wavelength of X-ray radiations, β is the full width at half of the maxima and θ is the Bragg's angle. Crystalline size is found to be 11 nm which is in great agreements with 14 nm reported by Almeida et al. [25] and less than 52 nm reported by Larbi et al. [22] for spray deposited NiMn₂O₄ thin films. The smaller crystalline size observed in present study is due to the different experimental conditions affecting growth of NiMn₂O₄ films.

3.2 Scanning electron microscopy

Surface morphology of spray deposited NiMn₂O₄ thin film is investigated using SEM. Figure 2 shows the SEM images of NiMn₂O₄ thin film at different magnifications. It shows fractured surface morphology; wherein small pores on the surface are covered by the particles. The image shows smaller uniformly distributed voids. These voids are interconnected and provide porous structure. These pores provide room to store the charge by faradaic redox reactions. Similar morphology was earlier reported for coprecipitated SnO₂ thin films by Chikhale et al. [26]. The

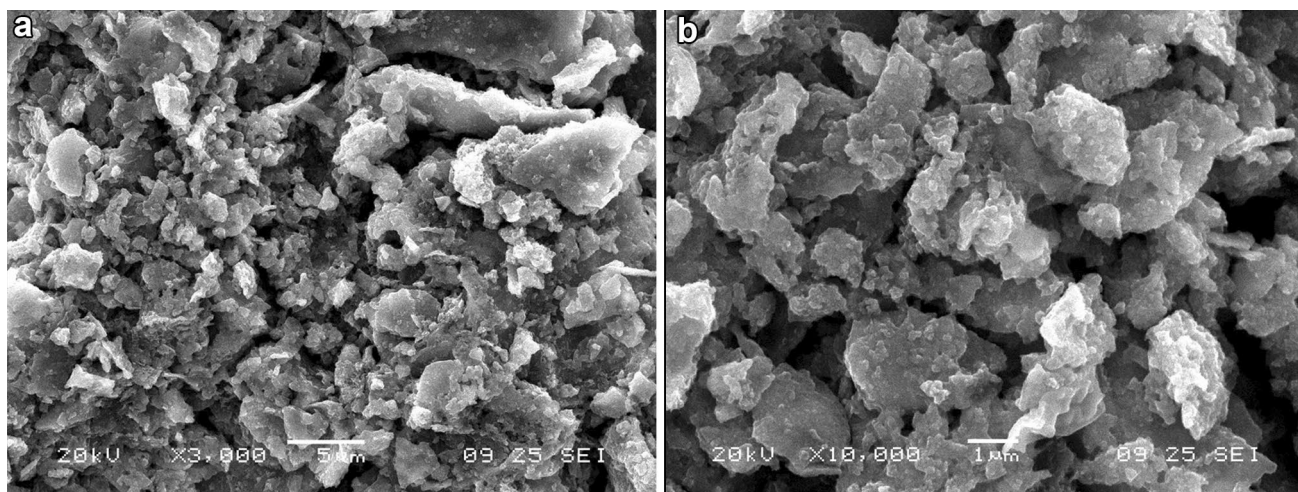


Fig. 2 SEM images of spray deposited NiMn₂O₄ thin films at magnification of **a** ×3000, **b** ×10,000 respectively

morphology observed in present study is different than the earlier reported for Hausmannite Mn_3O_4 thin films [27].

3.3 Optical absorption

Optical absorption spectra measured in the wavelength range 300–1100 nm, is used for determine the band gap of $NiMn_2O_4$ thin films. Absorption coefficient (α) is further used to evaluate the band gap of the $NiMn_2O_4$ using the relation [28],

$$\alpha = A \frac{(E_g - h\nu)^n}{h\nu} \tag{3}$$

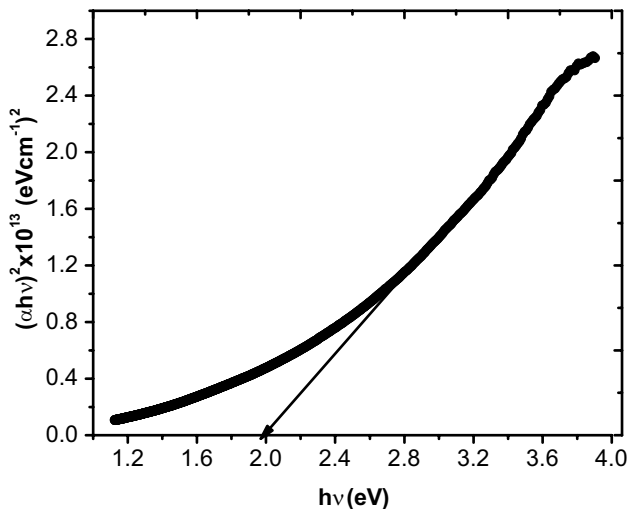


Fig. 3 Tauc plot $(\alpha h\nu)^2$ versus $h\nu$ for $NiMn_2O_4$ thin film spray deposited at $400\text{ }^\circ\text{C}$

where $h\nu$ is the energy of the incident photon, E_g is the band gap energy and $n = \frac{1}{2}$ or 2 for direct or indirect allowed transitions respectively. The absorption coefficient is found to be of the order of 10^5 cm^{-1} . Figure 3 shows the plot of $(\alpha h\nu)^2$ versus $h\nu$ for spray deposited $NiMn_2O_4$ thin film. The linear nature of the curve at absorption edge indicates direct allowed transition. The linear portion is extrapolated to real axis at $\alpha = 0$, intercept of which gives the band gap energy. Band gap energy for $NiMn_2O_4$ film is found to be 1.98 eV, which is lower than the pristine Mn_3O_4 and NiO thin films reported earlier [27, 29]. This band gap energy is comparable to the band gap energy reported by Zhang et al. [19]. This value of band gap energy is higher than 1.07 eV reported by Larbi et al. for $NiMn_2O_4$ [30], which is attributed to the presence of holes created by Ni ions replacing those of Mn in the lattice [30].

3.4 Electrochemical characterization

3.4.1 Cyclic voltammetry (CV)

The electrochemical performance of spray deposited $NiMn_2O_4$ thin film is studied in three electrode systems using electrochemical analyzer provided by CH instruments with $NiMn_2O_4$ as a working electrode, platinum wire as counter electrode and $Ag/AgCl$ as a reference electrode. The 2 M aqueous KOH was used as an electrolyte. The measurements are carried out in the potential window from -0.2 to 0.4 V. Fig. 4a gives the CV curves for $NiMn_2O_4$ electrode at various scan rates. From shape and symmetry of curve, it is concluded that the $NiMn_2O_4$ electrode shows an ideal electrochemical capacitive behavior.

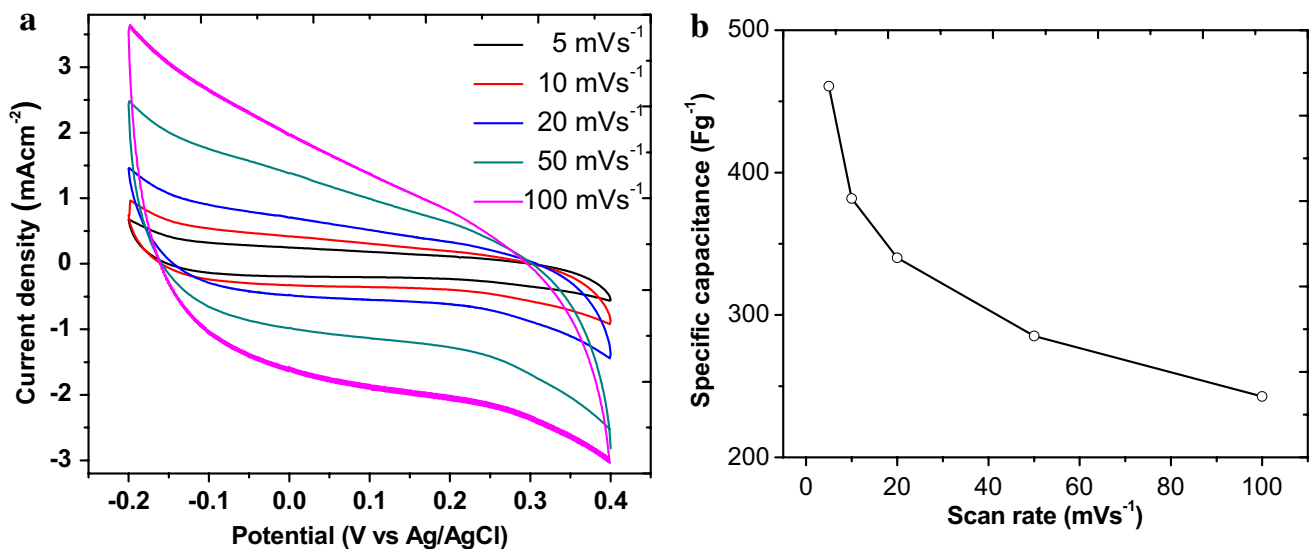


Fig. 4 **a** Cyclic voltammetry curves at various scan rates and **b** plot of specific capacitance versus scan rate for $NiMn_2O_4$ thin film electrode

The symmetry and quick reverse of current during potential inversion indicates fast charge transfer at the electrode surface. Absence of any peaks specifies pseudo constant charging and discharging over the complete voltammetry cycle. The probable charge storage mechanism may be explained as [15];



CV curves are used to estimate the specific capacitance (C_{sp}) of NiMn_2O_4 film at various scan rates by using equation [31];

$$C_{sp} = \frac{1}{m\nu(V_c - V_a)} \int_{V_a}^{V_c} I(V)dV \quad (5)$$

where, ν is the potential scan rate, $(V_c - V_a)$ is an operational potential window, I is the current and m is deposited mass of NiMn_2O_4 on 1 cm^2 surface of FTO coated glass substrate. The maximum specific capacitance is found to be 460 Fg^{-1} at the scan rate 5 mVs^{-1} . This value of specific capacitance is higher than that of Mn_3O_4 (394 Fg^{-1}) and NiO (405 Fg^{-1}) [27, 29] is reported that the addition of nickel into manganese based oxide enhances the ionic diffusivity and electrochemical performance [16]. The effect of scan rate on the specific capacitance is observed from Fig. 4b. It is seen that the specific capacitance decreases from 460 to 242 Fg^{-1} with increase in scan rate from 5 to 100 mVs^{-1} . At higher scan rate, electrolyte ions does not get sufficient time to diffuse into the pores of the material and therefore charges accumulate only on the outer surface of the electrode hence capacitance decreases. The specific capacitance observed in present study is better than specific capacitance reported in the literature. The porous NiMn_2O_4 electrode synthesized by calcining oxalate precursors in the air has delivered maximum specific capacitance of 180 Fg^{-1} at 5 mVs^{-1} scan rate [32]. Liu et al. [33] have reported nanostructured nickel–manganese oxide composite with specific capacitance of 453 Fg^{-1} at 10 mVs^{-1} scan rate.

3.4.2 Galvanostatic charge/discharge

Further, electrochemical performance of NiMn_2O_4 electrode is tested by galvanostatic charge/discharge study. Figure 5a shows the charge/discharge cycles for NiMn_2O_4 electrode at various current densities within the potential window -0.2 to 0.2 V in 2 M aqueous KOH electrolyte. It is observed that curves are symmetric and linear with respect to time confirming pseudocapacitive nature of the material. Sudden drop in the potential at the starting of discharge cycles is due to the small equivalent series

resistance of the electrode. The specific capacitance, specific energy and specific power of NiMn_2O_4 electrodes at various current densities are evaluated by using the following relations [34];

$$C_s = \frac{I \times \Delta t}{m \times \Delta V} \quad (6)$$

$$\text{SE} = \frac{1}{2} CV^2 \quad (7)$$

$$\text{SP} = \frac{3600 \times \text{SE}}{t} \quad (8)$$

where I is charge/discharge current at a discharge time t (s), ΔV is the potential window, and 'm' is the mass of the NiMn_2O_4 electrode. Specific capacitance calculated at current density of 2 Ag^{-1} is found to be 455 Fg^{-1} and corresponding specific energy and specific power are found to be 36.65 Whkg^{-1} and 1.54 kWkg^{-1} respectively. The values of specific capacitance, specific energy and specific power at various current densities are shown in Table 2.

Figure 5b represents the Ragone plot for NiMn_2O_4 electrode. The cycling stability is a basic need of supercapacitor electrode in practical use. Figure 5c shows the capacitance retention curve for NiMn_2O_4 electrode over 1000 charge–discharge cycles at a constant current density 2 Ag^{-1} . It is observed that there is only 7.03% reduction in specific capacitance after the 1000 charge/discharge cycles.

3.4.3 Electrochemical impedance spectroscopy (EIS)

The EIS is another important tool to inspect the electrochemical performance of the NiMn_2O_4 electrode. In order to evaluate the electronic and ionic conductivity of the NiMn_2O_4 electrode electrochemical impedance spectroscopy measurements are carried out in 2 M aqueous KOH within the frequency range 1 – 100 kHz . Figure 6 shows the Nyquist plot of NiMn_2O_4 electrode before and after 1000 charge/discharge cycles. In general the Nyquist plot is divided into three parts; high frequency region, middle frequency region and low frequency region [35]. In high frequency region, first non-zero intercept to the real axis gives the solution resistance (R_s), while the diameter of semicircle in middle frequency region gives charge-transfer resistance (R_{ct}) [36]. The values of R_s and R_{ct} for NiMn_2O_4 observed from Nyquist plots are 0.3Ω and $17.12 \Omega\text{cm}^2$ respectively. After completing 1000 charge/discharge cycles charge transfer resistance changes from 17.12 to $19.27 \Omega\text{cm}^2$. This contributes to reduce in specific capacitance (about 7.03% after 1000 cycles) showing long term cyclic stability. A more vertical line leaning to imaginary

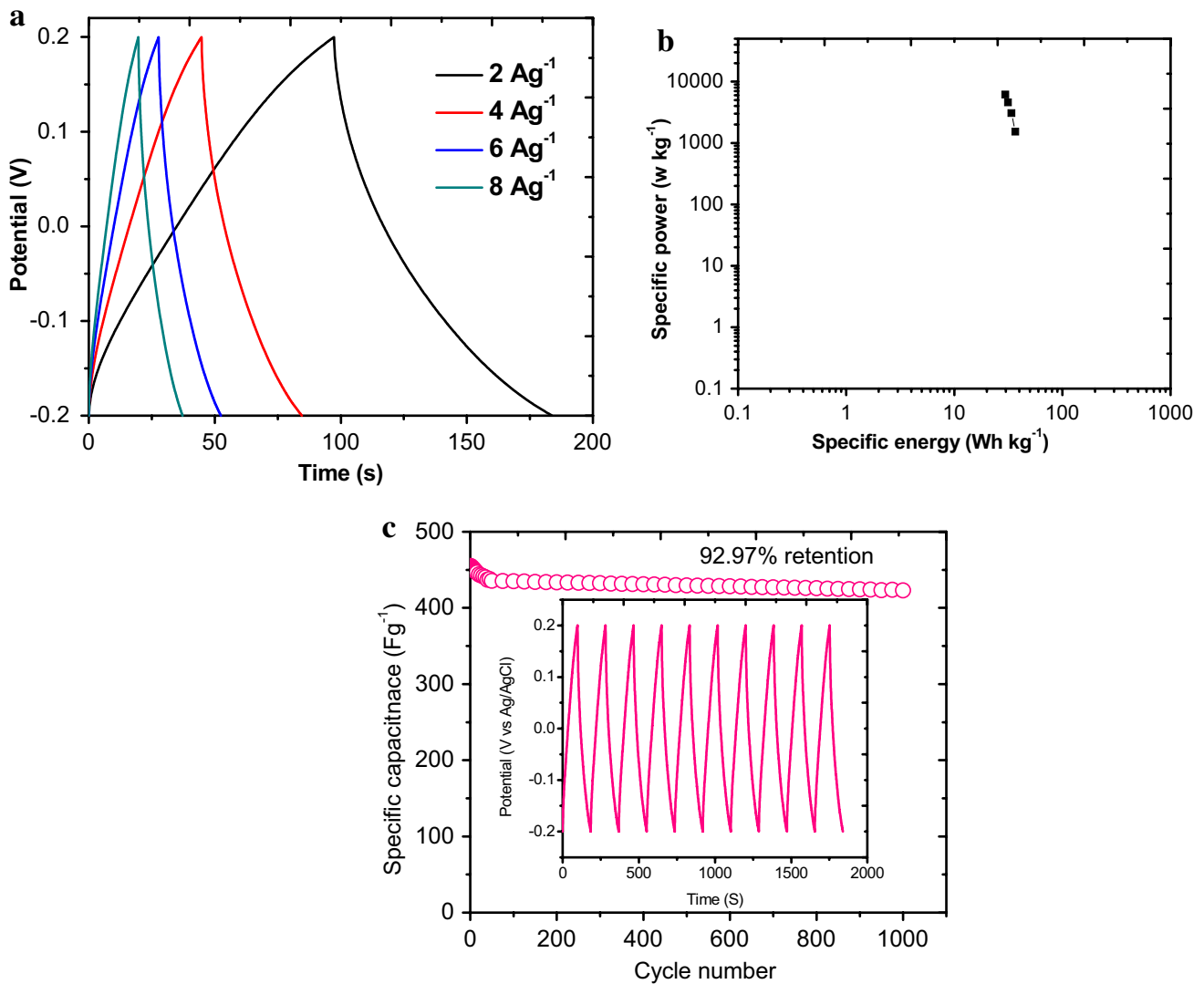


Fig. 5 Galvanostatic charge/discharge performance of NiMn₂O₄ electrode **a** charge/discharge curves at various current densities, **b** Ragone plot, **c** cycle stability at a constant current density of 2 Ag⁻¹

(inset shows the first 10 galvanostatic charge/discharge cycles at a current density of 2 Ag⁻¹)

Table 2 Specific capacitance, specific energy and specific power for mixed nickel manganese oxide electrode at different current densities

CD (Ag ⁻¹)	Cs (Fg ⁻¹)	SE (Whkg ⁻¹)	SP (kWkg ⁻¹)
2	458	36.65	1.54
4	421	33.72	3.07
6	392	31.36	4.61
8	370	29.67	6.14

CD charge/discharge current density, Cs specific capacitance, SE specific energy, SP specific power

axis suggests the lower diffusive resistance, which concludes good electrochemical reversibility of NiMn₂O₄ electrode [37].

4 Conclusions

Mixed nickel manganese oxide thin films have been successfully synthesized using computerized spray pyrolysis technique. XRD pattern reveals cubic NiMn₂O₄ as prominent phase. The fractured surface morphology containing small pores on the surface is observed from SEM. Optical band gap is found to be 1.98 eV. From cyclic voltammetry study, the maximum specific capacitance is found to be 460 Fg⁻¹ at scan rate of 5 mVs⁻¹. The galvanostatic charge–discharge study reveals long term stability with specific energy of 36.65 Whkg⁻¹ and specific power of 1.54 kWkg⁻¹. Electrochemical impedance spectroscopy measurements give low solution resistance and charge

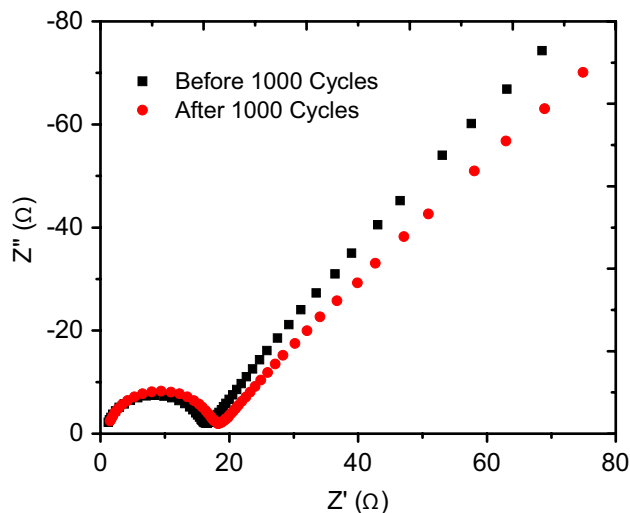


Fig. 6 Nyquist plots for NiMn_2O_4 electrode before and after 1000 charge/discharge cycles

transfer resistance. These results suggest that NiMn_2O_4 is good candidate for next generation energy storage devices.

Acknowledgements “Dr. A. A. Yadav is grateful to the Science and Engineering Research Board, Department of Science and Technology, New Delhi, India for the financial assistance through the Project under the SERC Fast Track Scheme for Young Scientist (File No. SB/FTP/PS- 068/2013).”

References

- P. Vigneshwaran, M. Kandiban, N. Senthil Kumar, V. Venkatchalam, R. Jayavel, I. VethaPotheher, *J. Mater. Sci.* **27**, 4653–4658 (2016)
- J. Yin, H. Zhang, J. Luo, M. Yao, W. Hu, *J. Mater. Sci.* (2016). doi:10.1007/s10854-016-5771-z
- Y. Tang, Y. Liu, S. Yu, W. Guo, S. Mu, H. Wang, Y. Zhao, L. Hou, Y. Fan, F. Gao, *Electrochim. Acta* **161**, 279–289 (2015)
- R.B. Pujari, V.C. Lokhande, V.S. Kumbhar, N.R. Chodankar, C.D. Lokhande, *J. Mater. Sci.* **27**, 3312–3317 (2016)
- W. Lan, G. Tang, Y. Sun, Y. Wei, P. La, Q. Su, E. Xie, *J. Mater. Sci.* **27**, 2741–2747 (2016)
- D.P. Dubal, A.D. Jagadale, S.V. Patil, C.D. Lokhande, *Mater. Res. Bull.* **47**, 1239–1245 (2012)
- M. Zhang, Q. Li, D. Fang, I.A. Ayhan, Y. Zhou, L. Dong, C. Xiong, Q. Wang, *RSC Adv.* **5**, 96205–96212 (2015)
- M. Gnerlich, H. Ben-Yoav, J.N. Culver, D.R. Ketchum, R. Ghodssi, *J. Power Sources* **293**, 649–656 (2015)
- A.A. Yadav, *J. Mater. Sci.* **27**, 1866–1872 (2016)
- J. Wang, Y. Zhang, P. Wan, T. Li, D. Hou, S. Hussain, H. Shao, *J. Mater. Sci.* **27**, 8020–8026 (2016)
- A.A. Yadav, *J. Mater. Sci.* (2016). doi:10.1007/s10854-016-5423-3
- M.H. Tahmasebi, K. Raeissi, M.A. Golozar, A. Vicenzo, M. Hashempour, M. Bestetti, *Electrochim. Acta* **190**, 636–647 (2016)
- D. Chen, Q. Wang, R. Wang, G. Shen, *J. Mater. Chem. A* **3**, 10158–10173 (2015)
- H.M. Lee, K. Lee, C.K. Kim, *Materials* **7**, 265–274 (2014)
- P. Ahuja, S.K. Ujjain, R.K. Sharma, G. Singh, *RSC Adv.* **4**, 57192–57199 (2014)
- H. Wei, J. Wang, L. Yu, Y. Zhang, D. Hou, T. Li, *Ceram. Int.* **42**, 14963–14969 (2016)
- M. Zhang, S. Guo, L. Zheng, G. Zhang, Z. Hao, L. Kang, Z.H. Liu, *Electrochim. Acta* **87**, 546–553 (2013)
- H. Goto, J. Fukushima, H. Takizawa, *Materials* **9**, 169–177 (2016)
- L.B. Zhang, Y. Hou, W. Zhou, Y.Q. Gao, J. Wu, Z.M. Huang, J.H. Chu, *Solid State Commun.* **159**, 32–35 (2013)
- S. Periyasamy, P. Subramanian, E. Levi, D. Aurbach, A. Gedanken, A. Schechter, *ACS Appl. Mater. Interfaces* **8**, 12176–12185 (2016)
- C.H. Wu, J.S. Ma, C.H. Lu, *Curr. Appl. Phys.* **12**, 1190–1194 (2012)
- T. Larbi, A. Amara, B. Ouni, A. Inoubli, M. Karyouli, A. Yumak, F. Saadallah, K. Boubaker, M. Amlouk, *J. Magn. Magn. Mater.* **387**, 139–146 (2015)
- C. Ma, Y. Liu, Y. Lu, H. Gao, H. Qian, J. Ding, *J. Mater. Sci.* **24**, 5183–5188 (2013)
- H. Gao, C. Ma, B. Sun, *J. Mater. Sci.* **25**, 3990–3995 (2014)
- J.M.A. Almeida, C.T. Meneses, A.S. de Menezes, R.F. Jardim, J.M. Sasaki, *J. Magn. Magn. Mater.* **320**, 304–307 (2008)
- L.P. Chikhale, J.Y. Patil, A.V. Rajgure, F.I. Shaikh, I.S. Mulla, S.S. Suryavanshi, *Measurement* **57**, 46–52 (2014)
- A.A. Yadav, S.N. Jadhav, D.M. Chougule, P.D. Patil, U.J. Chavan, Y.D. Kolekar, *Electrochim. Acta* **206**, 134–142 (2016)
- A.A. Yadav, *J. Mater. Sci.* **25**, 1251–1257 (2014)
- A.A. Yadav, U.J. Chavan, *J. Electroanal. Chem.* **782**, 36–42 (2016)
- T. Larbi, L. Ben said, A. Ben daly, B. oui, A. Labidi, M. Amlouk, *J. Alloys Compd* **686**, 168–175 (2016)
- A.A. Yadav, T.B. Deshmukh, R.V. Deshmukh, D.D. Patil, U.J. Chavan, *Thin Solid Films* **616**, 351–358 (2016)
- H. Pang, J. Deng, S. Wang, S. Li, J. Du, J. Chen, J. Zhang, *RSC Adv.* **2**, 5930–5934 (2012)
- E.H. Liu, W. Li, J. Li, X.Y. Meng, R. Ding, S.T. Tan, *Mater. Res. Bull.* **44**, 1122–1126 (2009)
- A.A. Yadav, *Thin Solid Films* **608**, 88–96 (2016)
- Y. Liu, D. He, H. Wu, J. Duan, *Integr. Ferroelectr.* **144**, 118–126 (2013)
- A.M. Patil, A.C. Lokhande, N.R. Chodankar, V.S. Kumbhar, C.D. Lokhande, *Mater. Des.* **97**, 407–416 (2016)
- M. Jlassi, I. Sta, M. Hajji, H. Ezzaouia, *Appl. Surf. Sci.* **308**, 199–205 (2014)